Colloids and Surfaces B: Biointerfaces 172 (2018) 10–16

Contents lists available at ScienceDirect

Colloids and Surfaces B: Biointerfaces

journal homepage: www.elsevier.com/locate/colsurfb

Kinetics and growth mechanism of the photoinduced synthesis of silver nanoparticles stabilized with lysozyme

Valentina Rey[a], Marcelo E. Gramajo Feijoo[b], Rodrigo E. Giménez[a,1], María E. Tuttolomondo[b], Faustino E. Morán Vieyra[a], Marcelo C. Sosa Morales[a], Claudio D. Borsarelli[a,*]

[a] Instituto de Bionanotecnología del NOA (INBIONATEC), Universidad Nacional de Santiago del Estero (UNSE), CONICET, RN9, km 1125, G4206XCP, Santiago del Estero, Argentina

[b] INQUINOA-CONICET, Instituto de Química Física, Facultad de Bioquímica, Química y Farmacia, Universidad Nacional de Tucumán, Ayacucho 471, T4000INI, San Miguel de Tucumán, Argentina

ARTICLE INFO

Keywords:
Photoreduction
Silver nanoparticles
Lysozyme
Nanoparticle growth
Aggregative-nucleation
Protein coating

ABSTRACT

A fast and single-step procedure is reported for the preparation of stable solutions of spherical-shaped silver nanoparticles (AgNPs) coated with lysozyme (LZ). The preparation of the AgNP@LZ nanocomposites was based on the reduction of Ag^+ with ketyl radicals photo-generated by the UVA-photolysis of the benzoin I-2959. Both reaction precursors bind to LZ, modifying its superficial charge and conformational structure. The photo-induced kinetics of formation of the AgNPs as a function of the LZ concentration was monitored in-situ by UV–vis absorption spectroscopy. The multivariate curve resolution-alternating least square (MCR–ALS) method was used for the deconvolution of the kinetic curves for each transient species formed before the growth of the final AgNPs colloids. The Kolmogorov-Johnson-Mehl-Avrami (KJMA) model to describe the formation of the AgNPs was used, and the respective first-order rate constants for the growth of the AgNPs as a function of the lysozyme concentration were calculated and the role of the protein capping in the growth kinetics was evaluated. Despite the protein being partially oxidized by the photo-generated radicals, it was strongly adsorbed onto the silver surface forming a tight coating shell around the AgNPs of approximately 30–60 protein molecules. As a result of the partial denaturation and crowded packing, its intrinsic lytic activity was strongly reduced.

1. Introduction

Supramolecular nanocomposites based on silver nanoparticles (AgNPs) show a current and increasing interest due to their applications in antibacterial devices [1], molecular and macromolecular sensing [2], enzyme immobilization [3], and plasmonic applications [4], among others.

For biological and medical applications, the study of the interactions of metal nanoparticles (MNPs) with proteins is essential, considering the intrinsic abundance and functionality of proteins in living tissues [5,6]. The biomacromolecule not only will play a key role in the stabilization of the MNPs, but also in cell metabolism and biodistribution of the nanocomposite in living organisms [6].

Some recent reports had described the formation and/or stabilization of AgNPs by different proteins [7], including human serum albumin [8–11], trypsin [11], and lysozyme [11–14]. Most of those studies have been focused on the bimolecular interaction of the protein with previously prepared MNPs, replacing the initial stabilizer molecule (*e.g.* citrate ion) by forming a protein supramolecular structure surrounding the AgNPs [9–11,13,14]. In the case of lysozyme, the protein has been also used as a photo-reductive agent by fluorescent light irradiation, promoting the reduction of Ag^+ to Ag° by oxidation of aromatic amino acid residues of the enzyme [13,15]. In this sense, light-induced processes emerge as a very versatile method for MNPs preparation due to the selective triggering and control of the reaction under mild conditions, the *in situ* generation of reducing agents, high spatial resolution, and low-time consuming [16,17]. However, the formation of MNPs is a kinetically complex process where several sequential nucleation-aggregation steps are occurring before the mature and stable MNPs are formed [18–20], and to the best our knowledge the protein effect on the growth kinetics of MNPs has not yet been extensively studied.

* Corresponding author.
E-mail address: cdborsarelli@gmail.com (C.D. Borsarelli).
[1] Present address: Instituto de Investigaciones Fisicoquímicas Teóricas y Aplicadas (INIFTA), Departamento de Química, Facultad de Ciencias Exactas, Universidad Nacional de La Plata, CONICET, Calle 64 y Diag. 113, 1900 La Plata, Argentina

https://doi.org/10.1016/j.colsurfb.2018.08.015
Received 31 March 2018; Received in revised form 7 August 2018; Accepted 9 August 2018
Available online 10 August 2018
0927-7765/

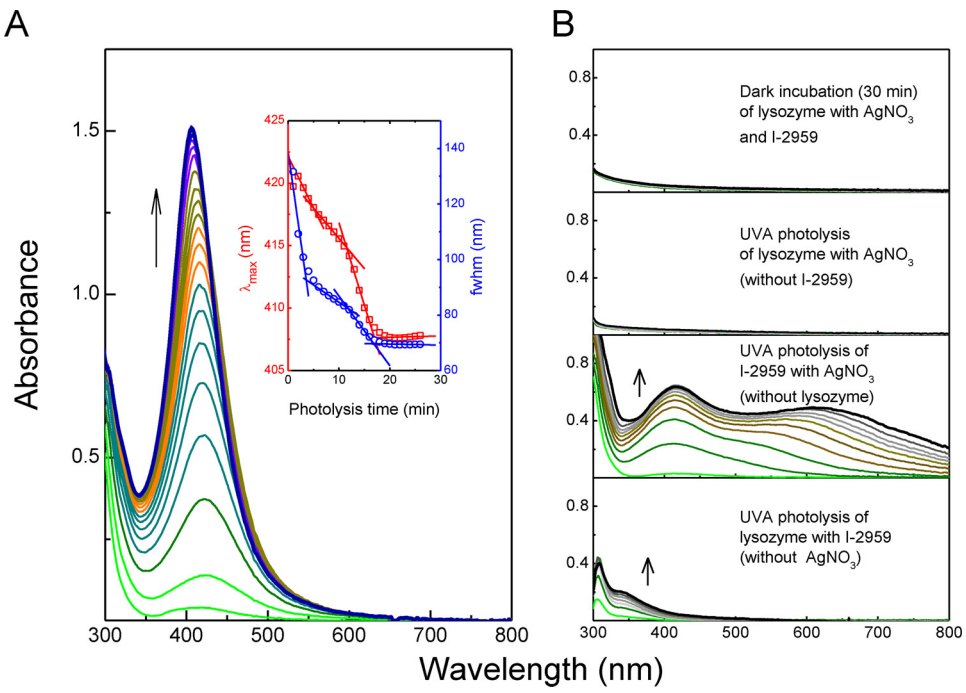

Fig. 1. UV–vis spectral changes produced during 25 min of UVA photolysis of aqueous solutions at 25 °C containing: **A**) 0.1 mM $AgNO_3$, 0.1 mM I-2959 and 1 μM Z. Inset: time-dependent changes of λ_{max} and fwhm during UVA-photolysis. **B**) Control experiments of mixtures of 0.1 mM $AgNO_3$, 0.1 mM I-2959, and/or 1 μM LZ under the reaction conditions indicated in the text of the figure.

Thus, in this report, we studied the *in situ* formation of AgNPs in the presence of lysozyme (LZ) as a model of biocompatible capping agent and its effect on the kinetics of formation AgNP@LZ nanocomposites and their structural properties. A simple "bottom-up" photochemical method for the preparation of the AgNP@LZ based in the reduction of Ag^+ cations by ketyl radicals generated by photo-cleavage of a water-soluble benzoin was used [7,9,17]. The kinetic and structural characterizations of the AgNP@LZ were performed by several spectroscopic and images techniques, combined with computational methods, and the obtained results indicated the fast formation of stable colloidal solutions of AgNPs coated with partially denatured protein molecules.

2. Materials and methods

2.1. Materials

Silver nitrate ($AgNO_3$), sodium citrate dihydrate ($C_6H_5Na_3O_7.2H_2O$), 2-hydroxy-4′-(2-hydroxyethoxy)-2-methylpropiophenone (I-2959), lysozyme (LZ, from chicken egg white, 58,100 units/mg) were purchased from Sigma-Aldrich. Ultra-pure water from a MiliQ system was used. Compressed ultrapure nitrogen (99,99%) was from Indura S.R.L. (Argentina).

2.2. Photoreductive synthesis of AgNPs

The reduction of Ag^+ was performed by ketyl radicals photo-generated by UVA-photolysis of the aqueous soluble benzoin I-2959 [17]. Details of the experimental set-up are given in the Supplementary Information file (SI).

2.3. Spectroscopic techniques

The UV–vis absorption and fluorescence spectra were registered using an OceanOptics USB2000 and Cary Eclipse instrument, respectively. Fluorescence lifetimes were obtained with the Tempro-01 spectrofluorometer (Horiba).

Circular dichroism (CD) spectra were registered with a Jasco J-810 spectropolarimeter, using a 0.1 cm path length quartz cell. The Raman spectra were recorded with a confocal Thermo Scientific DXR Raman microscope equipped with a high-resolution motorized platen, using gold-coated sample slides, and a laser power of 10 mW at 532 nm.

The attenuated total reflection Fourier-transform infrared (ATR-FTIR) spectra of dry sample films were obtained with a Jasco FT/IR-4600 apparatus at room temperature and under air-purged atmosphere (Parker Balston 75-45).

2.4. Dynamic light scattering measurements

Particle hydrodynamic diameters and zeta potential (ζ) were determined using the Horiba SZ-100 particle size analyser, with a 532 nm CW laser focused at 173° relative to the detection device. The data were analyzed with the Horiba NextGen Proyect^{TM} SZ-100 software.

2.5. Transmission electron microscopy (TEM)

The nanoparticles images were obtained with a Jeol 100 CX II TEM. Dilute sample solutions were evaporated onto a carbon-coated copper mesh grid. The ImageJ^{TM} free software was used to calculate particle size distribution from the micrographs. Information on mean size and standard deviation (SD) was calculated from at least four different regions in random fields of view.

2.6. Protein oxidation analysis

The extent of lysozyme oxidation elicited during the photoinduced formation of AgNPs was assessed by determination of both carbonyl and peroxide content (see SI). Proteolytic and/or crosslinking effects were evaluated by polyacrylamide gel electrophoresis in the presence of sodium dodecyl sulfate (SDS-PAGE), as described in SI.

2.7. Lysozyme lytic activity assay

It was determined by the turbidimetric *Micrococcus lysodeikticus* (ATCC 4698) assay [21], as briefly described in SI.

3. Results and discussion

3.1. Spectroscopic and structural characterization

Fig. 1A shows the time-resolved UV–vis spectral changes elicited during the UVA (350 ± 48 nm) photolysis of an aqueous solution containing 0.1 mM $AgNO_3$, 0.1 mM I-2959, and 1 μM LZ under N_2-atmosphere at room temperature (for details see SI). During irradiation, the original transparent solution progressively turned yellowish due to the growth of the typical surface plasmon resonance (SPR) band of AgNPs with absorption maximum (λ_{max}) at ≈400 nm, which is typical for the formation of low size spherical shaped AgNPs, *e.g.* < 20 nm diameter [7,9,22].

The variation of both λ_{max} and full width half maximum (fwhm) with the photolysis time showed three slopes changes before the stabilization of the SPR band (inset Fig. 1A), suggesting the formation of several transient spectroscopic species during the photogeneration of AgNP@LZ. In all cases, the spectra of the AgNP@LZ solutions did not show any red-shifted extra band, which rules out the presence of nanoparticle aggregates [22]. Similar results were obtained using 1 mM citrate as the stabilizer (AgNP@CIT, Figure S2 of SI). However, it may be noted that stable AgNPs colloidal solutions were obtained at a much lower concentration of LZ than for CIT (*e.g.* $10^2 \leq [CIT]/[LZ] \leq 10^4$), as it was previously reported for AgNPs stabilized with type I collagen and human serum albumin [7,9]. These results suggest that proteins are efficient stabilizers of MNPs. However, the AgNP@LZ showed SPR absorption bands more red-shifted and broader than those of AgNP@CIT (Table 1). This feature can be associated with the modification of the local nano-environment sensed by the SPR band due to the tight adsorption of the lysozyme onto the metal surface [12]. A similar result has also been observed for AgNPs stabilized with HSA [7,9], confirming the sensing ability of the SPR band of AgNPs of environmental changes [22].

Fig. 1B shows the UV–vis spectral changes produced under different reaction conditions. In the absence of UVA radiation, the reaction mixture did not produce AgNPs. The same happened during the UVA photolysis of a solution of LZ with $AgNO_3$ but without the radical initiator I-2959, since the protein does not absorb UVA. Hence, it was confirmed that the formation of the AgNP@LZ was only initiated by the ketyl radicals produced by the photo-cleavage of the benzoin [17]. On the other hand, during the UVA-photolysis of I-2959 in the presence of only $AgNO_3$ the prompt growth of the SPR band of AgNPs at 420 nm followed by the slower evolution of a band at 700 nm was observed. This behaviour is characteristic of a nanoparticle aggregation process, yielding an unstable colloid of greyish colour formed by the massive precipitation of silver particles [22]. This result confirms that both I-2959 and their photodegradation products are unable to stabilize the AgNPs under the used experimental conditions. Thus, the above results confirm that the enzyme is only acting as a stabilizer of the nascent AgNPs, but not as a reducing agent of Ag^+.

However, the photolysis of I-2959 only in the presence of LZ resulted in the growth of a new absorption band above 300 nm. At the same time, the intrinsic fluorescence emission band of the protein obtained with excitation at 280 nm decreased with the simultaneous growth of a new fluorescence band with a maximum at 460 nm (Figure S3 A of SI). The shape of the fluorescence excitation spectrum monitored at 460 nm was the same as that of the UV–vis spectrum, while the emission spectrum excited at 360 nm showed a single band with a maximum at 455 nm (Figure S3B of SI). The same protein fluorescence pattern was observed in the AgNP@LZ.

These spectral features are corresponding to those for the formation of kynurenine and/or *N*-formylkynurenine as side-chain oxidation products of LZ [23], due to the of peroxyl radical-mediated oxidation of the indole moiety of Trp residues by adding an extra carbonyl group. The formation of peroxyl radicals is plausible even in the presence of oxygen traces by its reaction with the substituted benzoyl radical produced during the photocleavage of I-2959 [7]. Effectively, after the UVA-photolysis of I-2959, the carbonyl content of the protein increased about five- and twenty-times for LZ and AgNP@LZ solutions, respectively (Table S1). However, no formation of protein peroxides and proteolysis/crosslinking products were observed (Figure S4 of SI). The latter result suggests that the primary structure of lysozyme was unchanged even with oxidized tryptophan residues, although secondary and tertiary structures could be modified after the reaction.

Fig. 2 shows the TEM micrographs confirming the formation of spherical AgNPs with metal core diameters (d_{TEM}) between 4 and 12 nm (Table 1). In turn, the DLS measurements yielded larger particle diameter values (d_{DLS}) than those calculated by TEM, in particular for the AgNP@LZ, due to the larger hydrodynamic size of LZ (*i.e.* 4.7 ± 2.5 nm as determined by DLS, data not shown). In fact, the coating thickness of the LZ shell around the AgNPs can be roughly estimated as $(d_{DLS} - d_{TEM})/2 = 5 \pm 2$ nm; a value similar to the protein dimensions in solution. The nanoparticle concentration of the AgNP@LZ solutions was calculated using the d_{TEM} values as described in section S3 of SI, and it varied approximately between 2 and 15 nM for the AgNP@LZ solutions prepared with 0.1 and 10 μM of LZ, respectively. Thus, by assuming a complete binding of the protein, the number of LZ molecules bound per AgNP was 53, 67, and 667 for the AgNP@LZ solutions prepared with 0.1, 1.0, and 10 μM of LZ, respectively (Table S2 of SI). However, besides of the full binding assumption, this estimation did not consider the available surface around the spherical AgNPs and neither the steric hindrance between neighboring protein molecules governed by the size of LZ, a prolate ellipsoid of 3 × 3 × 4.5 nm [24]. Hence, we used a simple 3D geometrical model for a more realistic estimation of the maximum range number of protein molecules that can be accommodated, considering the spherical metal core in the center of a geometrical figure, whose vertices represent the center of each protein unit [8] (Section S3 of SI). As a consequence, it was estimated that up to a maximum of 60 lysozyme molecules can be accommodated around a metal core of 6 nm of diameter, a similar number to that calculated from the concentration ratio between LZ/AgNP in solutions with 1 μM of protein. Therefore, for a 15 nM AgNP@LZ solution, the total protein concentration attached to the metal core is approximately 1 μM, suggesting that under the photo-stationary conditions used for the ketyl

Table 1
UV–vis spectral parameters and size properties of AgNPs, obtained by UVA-photolysis of aqueous solutions of 0.1 mM $AgNO_3$ and 0.1 mM I-2959 in presence of lysozyme or citrate as stabilizer agent. All measurements were carried out at 25 °C by triplicate and error bars corresponded to the ± SD of the mean value measured.

[Lysozyme] (μM)	λ_{max} (nm)	fwhm (nm)	d_{TEM} (nm)	d_{DLS} (nm)	ζ (mV)
0.1	412 ± 2	86 ± 3	12 ± 6	5 ± 2/16 ± 4/116 ± 60	+77 ± 11
0.5	406 ± 1	76 ± 2			
1.0	406 ± 1	70 ± 1	6 ± 1	19 ± 4	+55 ± 3
2.5	407 ± 1	68 ± 1			
5.0	406 ± 1	70 ± 2			
10.0	408 ± 1	73 ± 2	6 ± 2	13 ± 4	+60 ± 1
1 mM citrate	391 ± 1	60 ± 1	4 ± 1	6 ± 2	−25 ± 2

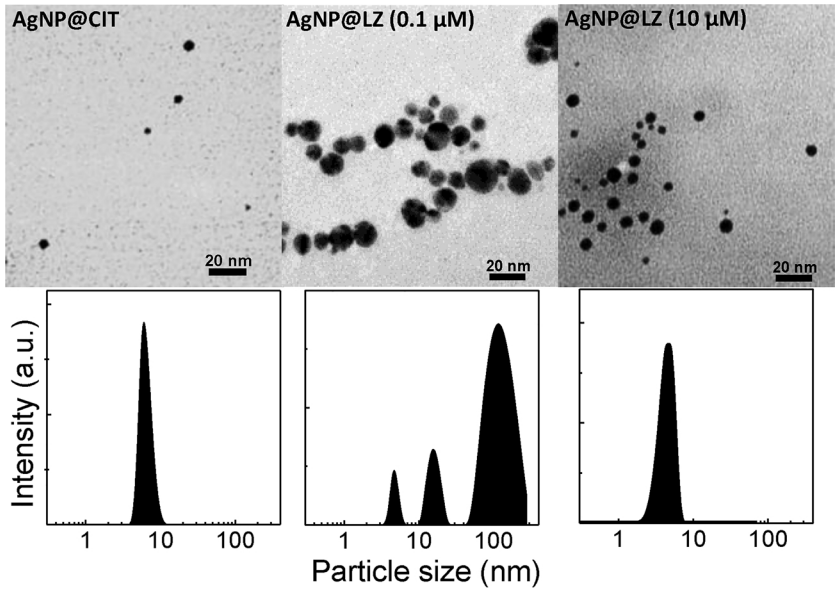

Fig. 2. TEM image (top) and particle diameter distribution by DLS measurements (bottom) for AgNPs prepared in presence of a) 1 mM citrate, and lysozyme b) 0.1 μM and c) 10 μM.

radical production, the coating efficiency of the AgNPs by LZ saturates at around 1 μM LZ. This result agrees with the constant values of λ_{max} and fwhm of the SPR band for AgNP@LZ formed with protein solutions in the concentration range between 1 and 10 μM (Table 1).

3.2. Growth mechanism for the formation of AgNP@LZ

In order to get a deeper information about the growth mechanism of the AgNPs, the UV–vis spectral evolution of the SPR band was analysed between 350–550 nm by multivariate curve resolution–alternating least square (MCR–ALS) method [25,26]. Fig. 3A shows a set of kinetic profiles for the relative absorbance (A_t/A_∞) of the four species components (named **1** to **4**) obtained with the MCR-ALS analysis for AgNP@LZ prepared with 5 μM LZ solution. The selection of at least four components in the MCR-ALS analysis was based on the number of linear regions observed in the plots of λ_{max} and fwhm *vs.* photolysis time (inset of Fig. 1A) and the obtention of optimum statistical results, *e.g.* lack of fit (LOF) and variance R^2 (Tables S4 and S5 of SI).

A Gaussian shape kinetic behaviour was observed for species called **1** to **3**, indicating their transient nature, since the decay of each species is coupled with the formation of the following one. Instead, the species **4** showed a sigmoidal-like kinetic profile, suggesting that it may be considered as the final AgNPs. The inset of Fig. 3A shows the associated normalized UV–vis spectrum to each species, confirming the blue-shifting and narrowing of the SPR band as the process progressed from the species **1** to **4**. Similar kinetic profiles were obtained in all cases (Figure S5 of SI).

The sum of the individual A_t/A_∞ values for species **1** to **4** (grey rhomboid curve) represents the kinetic profile of the global process, with a sigmoidal shape typical of an aggregation-nucleation growth process [19,20,27]. Thus, our results can fit with a formation mechanism composed of at least three transient nucleation steps previous to the last aggregative growth step to yield the final species **4**, Scheme 1.

Among the several mechanisms that describe the growth of MNPs [20], the Kolmogorov-Johnson-Mehl-Avrami (KJMA) model has been suitable for the modeling of the growth kinetics of MNPs solutions with different capping agents [19,27]. The KJMA model describes the particle growth by the sigmoidal-like Eq. (1), where k_g is the first-order rate constant of particle growth and n is the Avrami exponent, which theoretical value lies between 1 and 4 depending on the nucleation

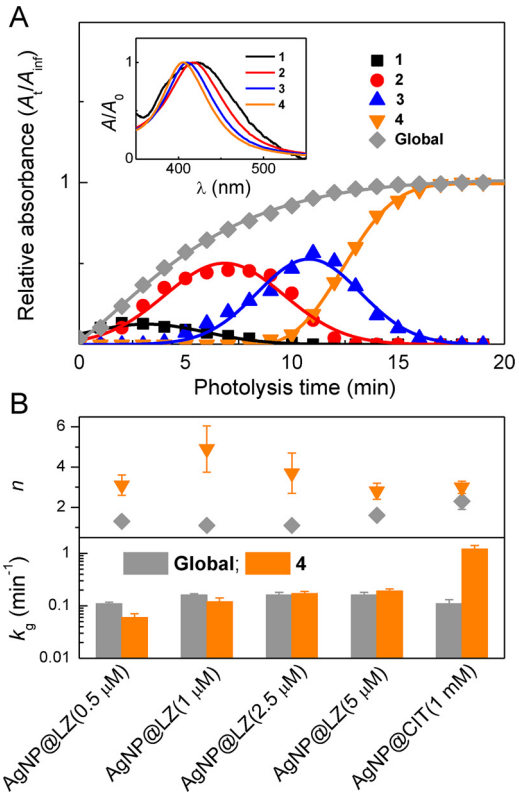

Fig. 3. A) Kinetic profiles of the four component species obtained by MCR-ALS analysis of the time-resolved UV–vis spectra during the photo-reductive generation of AgNPs in the presence of 5 μM LZ at 25 °C. Inset: Normalized absorbance spectrum of each kinetic species. **B)** Growth rate constant (k_g) and Avrami's exponent (n) values together with the respective ± SD values calculated by the fitting of the kinetic curves using Eq. (1) (KJMA model).

$$I-2959 \xrightarrow{UVA} R^{\bullet} \xrightarrow{Ag^+} nAg^0 \xrightarrow{nucleation1} 1 \xrightarrow{nucleation2} 2 \xrightarrow{nucleation3} 3 \xrightarrow{growth} 4$$

Scheme 1. Sequential nucleation-aggregative growth model for the reductive synthesis of AgNPs by UVA-photolysis of I-2959 as source of ketyl radicals (R·).

mechanism and the dimensionality of the particle growth [28].

$$\frac{A_t}{A_\infty} = 1 - \exp(k_g t)^n \quad (1)$$

Satisfactory fittings of the global growth process of AgNPs were obtained, as indicated by the solid grey line in Fig. 3A and the fitted data values are reported in Table S3 of SI. Fig. 3B compares n and k_g values for the global growth of the different preparations of AgNPs, and they were quite independent on the nature of the stabilizer, *e.g.* CIT or LZ, and also insensitive to the variation of the protein concentration. This can be the result of the convolution of the steps for nucleation (Gaussian curves) and growth (sigmoidal curve) processes [27], compensating rate differences between individual steps and yielding average values of both n and k_g. Similar values applying the KJMA model were also obtained for the thermal synthesis of AgNPs at 130 °C [19] and AuNPs at 180 °C [27], confirming that the KJMA-model is appropriate to describe the formation of MNPs by both thermal and photochemical radical-mediated processes.

The splitting of kinetic profiles of each species obtained by the chemometric MCR-ALS method allowed the fitting with Eq. (1) of the sigmoidal growth of the final species **4**, and their respective n and k_g values are presented in Fig. 3B (orange symbols and bars). An average value of $n = 3.5 \pm 0.7$ was obtained, accordingly with the expected theoretical value $n = 4$ for a spherical growth of the particle with a constant nucleation rate [28]. Now, the calculated k_g for the formation of species **4** was one-order of magnitude larger by using CIT than LZ as the stabilizer (Fig. 3B), indicating a kinetic-driven difference given by the nature of the stabilizer. According to Scheme 1, the step from species **3** to **4** represents the coalescence process of the final crystal seeds produced in the previous nucleation steps. For MNPs, this coalescence step is suddenly produced when a critical concentration of crystal seeds is reached [18,20,29,30]. Thus, the larger k_g value for the formation of AgNP@CIT than AgNP@LZ can be related with the minor energy barrier for the coalescence of the nanoparticle capped with citrate (only stabilized by electrostatic repulsion, $\xi = -25$ mV) than with LZ (stabilized by both electrostatic repulsion, $\xi = +55$ mV, and steric effects) [20,29].

For the transient species, **1**, **2**, and **3** the fitting with the Gaussian Eq. (2) allowed the calculation of the nucleation time t_n at the curve maximum, the time-window of nucleation Δt_n, and the total curve area A [19,20,27].

$$\frac{A_t}{A_\infty} = \frac{A}{\Delta t_n \sqrt{\pi/2}} \exp\left[-2\frac{(t-\tau_n)^2}{\Delta t_n^2}\right] \quad (2)$$

Table S3 of SI shows that both t_n and Δt_n values for the transient species **1** to **3** for AgNP@LZ were reduced with the increment of enzyme concentration, indicating that the transient nucleation steps are controlled by the protein. In the case of the AgNP@CIT, the subsequent nucleation steps were accelerated as the process goes forward probably driven by mild electrostatic repulsions.

3.3. Effects on the structure and lytic activity of lysozyme

The large molar excess used for the precursor reactants I-2959 and Ag^+ compared with the amount of LZ used as the stabilizing agent can affect both the structure and functionality of the protein. The interaction of both reactants with the protein was evaluated by the fluorescence quenching of LZ by Ag^+ and I-2959 (Fig. 4). The intrinsic fluorescence of LZ is mainly due to the solvent-exposed Trp62 and Trp108 residues, both on each side of the active site [33]. The fluorescence intensity values were corrected by primary and secondary inner filter effects and the protein fluorescence lifetimes were fitted with a three-exponential decay function. The average lifetime values were calculated using the fractional fluorescence contribution of each component [31], and in the absence of quenchers $\tau_0 = 1.68 \pm 0.06$ ns was

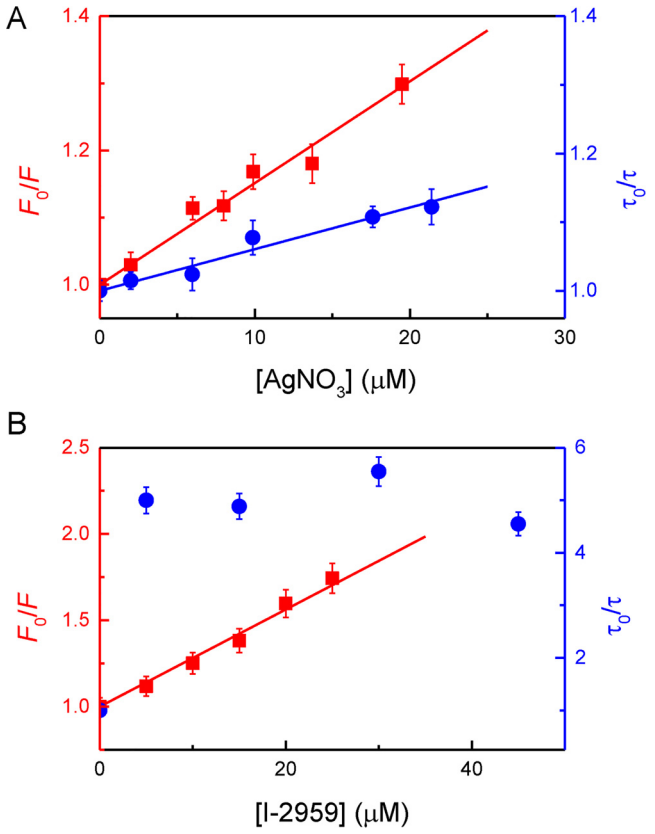

Fig. 4. Stern-Volmer plots for the steady-state (F_0/F) and dynamic (τ_0/τ) quenching of the intrinsic fluorescence of 10 μM lysozyme by: **A**) $AgNO_3$, and **B**) I-2959. In all cases excitation was performed at 295 nm and emission collected at 340 nm. Experiments were done by duplicate at 25 °C, and the error bar represents the mean absolute deviation of each average value.

obtained. In the quenching by Ag^+, the slope of the F_0/F data was larger than that for τ_0/τ (Fig. 4A), indicating the existence of a combined static-dynamic fluorescence quenching mechanism [31]. Therefore, in order to separate the static and dynamic quenching components, the quenching data was re-plotted with Eq. (3) assuming the formation of a 1:1 ground state complex between the Trp residues and Ag^+ with an association constant K_a [31].

$$\frac{F_0}{F} \times \frac{\tau}{\tau_0} = 1 + K_a[Q] \quad (3)$$

The $K_a = 8150 \pm 120\ M^{-1}$ was obtained by linear fitting of the fluorescence data with Eq. (3) (Figure S6 of SI), similar to $K_a = 6500\ M^{-1}$ calculated for the formation of the 1:1 complex between the free amino acid Trp and Ag^+ [32]. The binding of Ag^+ to the protein was also evidenced by the increases of the ζ-potential value from $+16 \pm 1$ mV to $+23 \pm 3$ mV of a 10 μM LZ solution after the addition of 110 μM Ag^+.

On the other hand, the fluorescence lifetime of the protein decreased to a constant value of 0.33 ns after the addition of I-2959 (Fig. 4B). This behavior can be associated with a static quenching process with some conformational change of the protein due to the tight binding of I-2959 modifying the nanoenvironment of the emitting Trp residues. Thus, the F_0/F was fitted with Eq. (3) considering $\tau_0/\tau = 1$, and an apparent binding constant of $K_a = 2.9 \times 10^5\ M^{-1}$ was obtained. Hence, the strong protein fluorescence quenching effect observed by adding either I-2959 or Ag^+ suggests that the active site of LZ can be affected.

In order to confirm if the presence of the precursor reactants induces conformational changes in the protein, attenuated total reflectance Fourier-transform infrared spectroscopy (ATR-FTIR) measurements

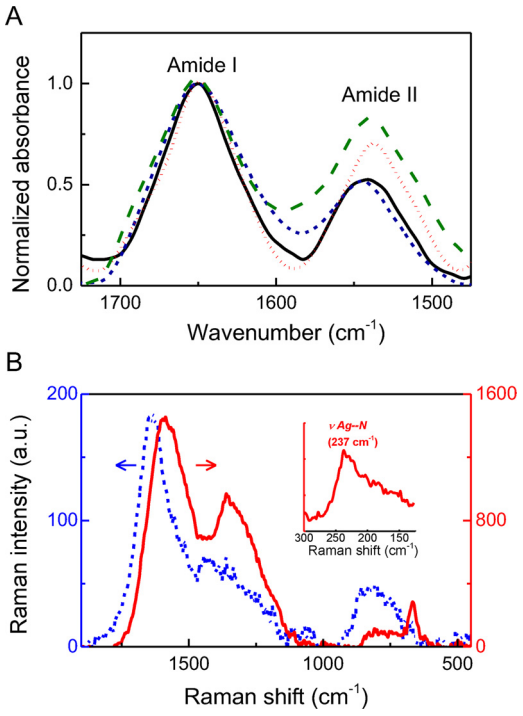

Fig. 5. A) Attenuated total reflection Fourier-transform infrared spectra of 10 μM lysozyme (black solid) under different mixture conditions with: (blue short-dashed) 0.1 mM I-2959; (red dotted) 0.1 mM Ag^+; and (green dashed) 0.1 mM I-2959 and 0.1 mM Ag^+. Three set of spectral measurements were averaged and smoothed (20 points) to minimize spectral noise. **B**) Raman spectra of 10 μM LZ (blue dashed) and AgNP@LZ solutions (red solid), the latter prepared from a 10 μM protein solution.

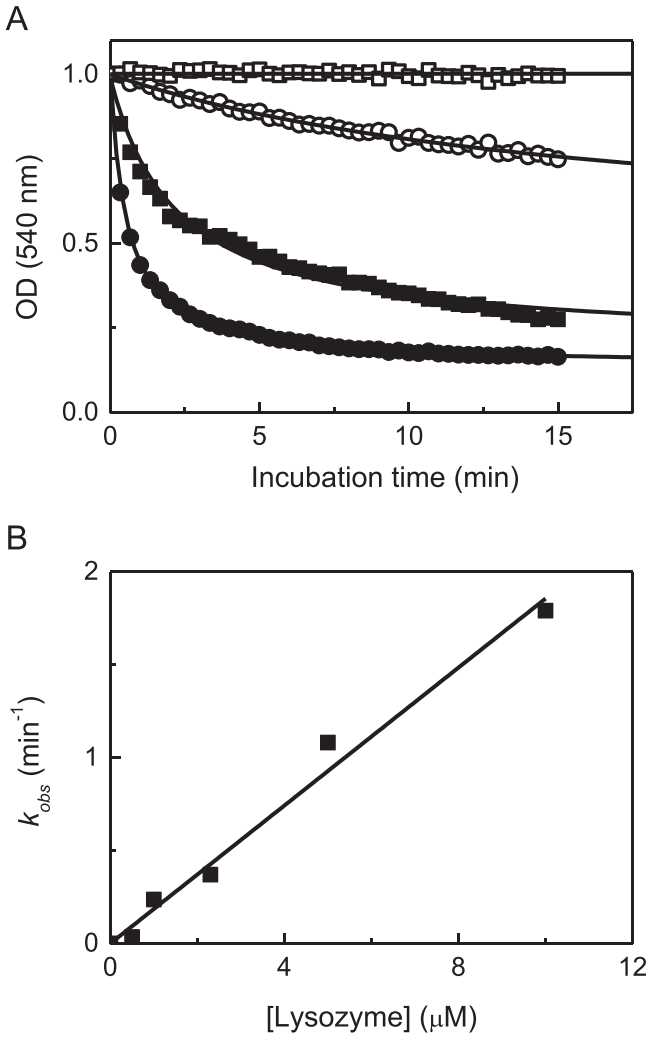

Fig. 6. A) Lytic kinetics of incubated cell suspensions of *Micrococcus lysodeikticus* at 25 °C monitored by the optical density (OD) at 540 nm in the presence of: (■) 2 μM LZ, (●) 10 μM LZ, (□) AgNP@LZ (2 μM), and (○) AgNP@LZ (10 μM). Solid lines represent the second-order fitting with Eq. (4). **B**) Variation of pseudo-first order rate constant (k_{obs}) *vs.* native lysozyme concentration.

were performed (Fig. 5A). Conformational protein can produce changes of shape and relative intensities of the typical Amide I (1700-1600 cm^{-1}) and Amide II (1625–1500 cm^{-1}), which are attributed to the stretching vibration modes of the C═O group of the peptide linkage, and the combination of N—H bending and C—N stretching, respectively [33]. The bandwidth of the Amide I band was increased about 12 cm^{-1} in the presence of I-2959, indicating an increase in the amount of the β-sheet structure. On the other hand, the addition of $AgNO_3$ increased the band ratio Amide II/Amide I as a result of the loss of α-helix structure [33]. Finally, the effect of both I-2959 and $AgNO_3$ on the ATR-FTIR spectrum of LZ was almost complementary, confirming that the protein was partially denatured previously to the *in situ* preparation of the AgNP@LZ.

Fig. 5B compares the Raman spectra of 10 μM LZ with that of AgNP@LZ prepared with a 10 μM LZ solution. For AgNP@LZ, a ten-times larger signal was observed due to the Surface Enhancement Raman Scattering (SERS) effect together with the appearance of a sharp band at 237 cm^{-1} (inset of Fig. 5B) due to the Ag–N vibrational mode [12,34]. The latter result is a clear fingerprint of the adsorption of LZ onto the metal surface through the N-atoms of the protein residues. The broadening and shifting of the Amide I band (1700-1600 cm^{-1} [12]) in the spectrum of AgNP@LZ, are indicative of strong intermolecular hydrogen bond interactions due to the denaturation of LZ [33]. Moreover, the depletion of the band at 805 cm^{-1} corresponds to the disruption of hydrogen bonding between the Trp residues and other residues of the peptide backbone, that together with the enhancement of the vibrational modes at 664 cm^{-1} associated with the C–S bond of cysteine residues also indicate conformational changes in the adsorbed protein [34].

The loss of native structure for LZ in AgNP@LZ was also evidenced by the circular dichroism spectral changes (Figure S7 of SI) since the ellipticity changes reflected the loss of the predominant α-helix structure of the native protein, concomitant with the increment of β-sheet conformation for the adsorbed protein [35]. Hence, the LZ is partially denatured forming the capping shell of the AgNP@LZ nanoparticles.

Due to the intrinsic antimicrobial activity of native LZ by the enzymatic hydrolysis of the peptidoglycan layer that surrounds the cell membrane, the capability of AgNP@LZ nanocomposites to cleavage the glycosidic bond in the alternating β-linked (1–4) copolymer of the N-acetyl-D-muramic acid was tested, by measuring the reduction of the optical density of the cell suspensions of *Micrococcus lysodeikticus* [21]. Fig. 6A shows the decreases of the optical density (OD) at 540 nm elicited by native LZ and AgNP@LZ at different protein concentrations. The kinetic curves were fitted with a second-order law regarding LZ [21], Eq. (4), and the pseudo first-order rate constant $k_{obs} = k_2[LZ]$ was calculated. For the native LZ a linear relationship of k_{obs} *vs.* [LZ] was obtained (Fig. 6B), supporting the second-order kinetic modelling, and the lytic activity rate constant $k_2 = 1.9 \times 10^5$ $M^{-1}\,min^{-1}$ was obtained.

$$OD_{(t)} = OD_{(\infty)} + \frac{OD_{(t)} - OD_{(\infty)}}{1 + k_{obs}t} \quad (4)$$

Only the AgNP@LZ nanocomposites prepared with 5 μM and 10 μM

LZ solutions showed measurable lytic activity, with k_{obs} values of 0.040 min^{-1} and 0.058 min^{-1}, respectively. By assuming the same lytic rate constant k_2 for the nanocomposites than for the native LZ, the effective concentration of lytic active sites in each AgNP@LZ solution was 211 nM and 305 nM, respectively. Considering that the concentration of AgNP@LZ was estimated at 15 nM, it can be speculated that between 14 and 20 protein molecules per AgNP@LZ retained its lytic activity.

4. Conclusions

The "bottom-up" method of reduction of Ag^+ by ketyl radicals photo-generated with the benzoin I-2959 [17] in the presence of lysozyme as stabilizer was evaluated, obtaining highly-stable AgNP@LZ colloids of spherical shape. The evolution of the SPR band of the nanocomposites was analysed by the multivariate curve resolution-alternating least square (MCR–ALS) method [26], allowing the separation of up to three-transient species before the final AgNPs were formed. The KJMA-model of aggregation-nucleation [19] was successfully used to characterize the role of the protein in the nucleation and growth of the AgNPs. Both the radical precursor I-2959 and Ag^+ tightly bind to the LZ, inducing a partial conformational change of the protein. The photocleavage of I-2959 to yield ketyl and benzoyl radicals also increases the carbonyl content of the protein with the formation of fluorescent oxidation products, such as side-chain kynurenine.

Hence, the nascent AgNPs are strongly coated with partially denatured LZ, driven by intense surface and hydrophobic forces, resulting in a large loss of the lytic activity of the enzyme. It is interesting to note that in the case of AgNP@LZ prepared by mixing native LZ with preformed AgNPs, the adsorbed protein was almost not denaturalized [11,13,14]. Thus, the properties of the protein coating around the MNPs can be tuned depending on the preparation method.

Acknowledgments

The Argentinean institutions Consejo Nacional de Investigaciones Científicas y Técnicas (CONICET, PIO-UNSE-2014-0012) and Fondo para la Investigación Científica y Tecnológica (FONCyT, PICT-2015-0828) supported this work. CDB also thanks to the Alexander von Humboldt Stiftung of Germany for an equipment grant (ATR-FITR Jasco 4600).

Appendix A. Supplementary data

Supplementary material related to this article can be found, in the online version, at doi:https://doi.org/10.1016/j.colsurfb.2018.08.015.

References

[1] A. Panáček, L. Kvítek, R. Prucek, M. Kolář, R. Večeřová, N. Pizúrová, V.K. Sharma, Tj. Nevěčná, R. Zbořil, Silver colloid nanoparticles: synthesis, characterization, and their antibacterial activity, J. Phys. Chem. B 110 (2006) 16248–16253.
[2] S. Guo, E. Wang, Functional micro/nanostructures: simple synthesis and application in sensors, fuel cells, and gene delivery, Acc. Chem. Res. 44 (2011) 491–500.
[3] S.A. Ansari, Q. Husain, Potential applications of enzymes immobilized on/in nano materials: a review, Biotechnol. Adv. 30 (2012) 512–523.
[4] M. Rycenga, C.M. Cobley, J. Zeng, W. Li, C.H. Moran, Q. Zhang, D. Qin, Y. Xia, Controlling the synthesis and assembly of silver nanostructures for plasmonic applications, Chem. Rev. 111 (2011) 3669–3712.
[5] M. Ahumada, E. Lissi, A.M. Montagut, F. Valenzuela-Henriquez, N.L. Pacioni, E.I. Alarcon, Association models for binding of molecules to nanostructures, Analyst 142 (2017) 2067–2089.
[6] M. Mahmoudi, I. Lynch, M.R. Ejtehadi, M.P. Monopoli, F.B. Bombelli, S. Laurent, Protein−nanoparticle interactions: opportunities and challenges, Chem. Rev. 111 (2011) 5610–5637.
[7] E.I. Alarcon, K. Udekwu, M. Skog, N.L. Pacioni, K.G. Stamplecoskie, M. Gonzalez-Bejar, N. Polisetti, A. Wickham, A. Richter-Dahlfors, M. Griffith, J.C. Scaiano, The biocompatibility and antibacterial properties of collagen-stabilized, photochemically prepared silver nanoparticles, Biomaterials 33 (2012) 4947–4956.
[8] M. Ahumada, C. Bohne, J. Oake, E.I. Alarcon, Protein capped nanosilver free radical oxidation: role of biomolecule capping on nanoparticle colloidal stability and protein oxidation, Chem. Commun. 54 (2018) 4724–4727.
[9] E.I. Alarcon, C.J. Bueno-Alejo, C.W. Noel, K.G. Stamplecoskie, N.L. Pacioni, H. Poblete, J.C. Scaiano, Human serum albumin as protecting agent of silver nanoparticles: role of the protein conformation and amine groups in the nanoparticle stabilization, J. Nanopart. Res. 15 (2013) 1374.
[10] M. Voicescu, S. Ionescu, D.G. Angelescu, Spectroscopic and coarse-grained simulation studies of the BSA and HSA protein adsorption on silver nanoparticles, J. Nanopart. Res. 14 (2012).
[11] V. Banerjee, K.P. Das, Interaction of silver nanoparticles with proteins: A characteristic protein concentration dependent profile of SPR signal, Colloids Surf. B Biointerfaces 111 (2013) 71–79.
[12] G. Chandra, K.S. Ghosh, S. Dasgupta, A. Roy, Evidence of conformational changes in adsorbed lysozyme molecule on silver colloids, Int. J. Biol. Macromol. 47 (2010) 361–365.
[13] D.M. Eby, N.M. Schaeublin, K.E. Farrington, S.M. Hussain, G.R. Johnson, Lysozyme catalyzes the formation of antimicrobial silver nanoparticles, ACS Nano 3 (2009) 984–994.
[14] G. Wang, H. Hou, S. Wang, C. Yan, Y. Liu, Exploring the interaction of silver nanoparticles with lysozyme: Binding behaviors and kinetics, Colloid Surf. B-Biointerfaces 157 (2017) 138–145.
[15] K. Umesh, K.R. Amaresh, S. Chandrashekhar, A.H. Anandwardhan, P. Archana, P. Pankaj, Green approach towards size controlled synthesis of biocompatible antibacterial metal nanoparticles in aqueous phase using lysozyme, Curr. Nanosci. 8 (2012) 130–140.
[16] M. Sakamoto, M. Fujistuka, T. Majima, Light as a construction tool of metal nanoparticles: synthesis and mechanism, J. Photochem. Photobiol. C-Photochem. Rev. 10 (2009) 33–56.
[17] J.C. Scaiano, P. Billone, C.M. Gonzalez, L. Maretti, M.L. Marin, K.L. McGilvray, N. Yuan, Photochemical routes to silver and gold nanoparticles, Pure Appl. Chem. 81 (2009) 635–647.
[18] J. Polte, X. Tuaev, M. Wuithschick, A. Fischer, A.F. Thuenemann, K. Rademann, R. Kraehnert, F. Emmerling, Formation mechanism of colloidal silver nanoparticles: Analogies and differences to the growth of gold nanoparticles, ACS Nano 6 (2012) 5791–5802.
[19] V.N. Richards, N.P. Rath, W.E. Buhro, Pathway from a molecular precursor to silver nanoparticles: the prominent role of aggregative growth, Chem. Mater. 22 (2010) 3556–3567.
[20] N.T.K. Thanh, N. Maclean, S. Mahiddine, Mechanisms of nucleation and growth of nanoparticles in solution, Chem. Rev. 114 (2014) 7610–7630.
[21] A.L.N. Prasad, G. Litwack, Measurement of the lytic activity of lysozymes (muramidases), Anal. Biochem. 6 (1963) 328–334.
[22] N.G. Bastús, F. Merkoçi, J. Piella, V. Puntes, Synthesis of highly monodisperse citrate-stabilized silver nanoparticles of up to 200 nm: kinetic control and catalytic properties, Chem. Mater. 26 (2014) 2836–2846.
[23] Y. Fukunaga, Y. Katsuragi, T. Izumi, F. Sakiyama, Fluorescence characteristics of kynurenine and *N*'-Formylkynurenine. Their use as reporters of the environment of tryptophan 62 in hen egg-white lysozyme, J. Biochem. 92 (1982) 129–141.
[24] M. Radmacher, M. Fritz, H. Hansma, P. Hansma, Direct observation of enzyme activity with the atomic force microscope, Science 265 (1994) 1577–1579.
[25] M. Garrido, F.X. Rius, M.S. Larrechi, Multivariate curve resolution–alternating least squares (MCR-ALS) applied to spectroscopic data from monitoring chemical reactions processes, Anal. Bioanal. Chem. 390 (2008) 2059–2066.
[26] J. Jaumot, R. Gargallo, A. de Juan, R. Tauler, A graphical user-friendly interface for MCR-ALS: a new tool for multivariate curve resolution in MATLAB, Chemometr. Intell. Lab. Syst. 76 (2005) 101–110.
[27] S.P. Shields, V.N. Richards, W.E. Buhro, Nucleation control of size and dispersity in aggregative nanoparticle growth. A study of the coarsening kinetics of thiolate-capped gold nanocrystals, Chem. Mater. 22 (2010) 3212–3225.
[28] T. Pradell, D. Crespo, N. Clavaguera, M.T. Clavaguera-Mora, Diffusion controlled grain growth in primary crystallization: avrami exponents revisited, J. Phys. Condens. Matter 10 (1998) 3833.
[29] J. Polte, Fundamental growth principles of colloidal metal nanoparticles – a new perspective, Cryst. Eng. Comm. 17 (2015) 6809–6830.
[30] M. Wuithschick, B. Paul, R. Bienert, A. Sarfraz, U. Vainio, M. Sztucki, R. Kraehnert, P. Strasser, K. Rademann, F. Emmerling, J. Polte, Size-controlled synthesis of colloidal silver nanoparticles based on mechanistic understanding, Chem. Mater. 25 (2013) 4679–4689.
[31] J.R. Lakowicz, Principles of Fluorescence Spectroscopy, 3rd edition ed., Springer Science + Business Media, LLC, Singapore, 2006.
[32] R.F. Chen, Quenching of the fluorescence of proteins by silver nitrate, Arch. Biochem. Biophys. 158 (1973) 605–622.
[33] M. Jackson, H.H. Mantsch, The use and misuse of FTIR Spectroscopy in the determination of protein structure, Crit. Rev. Biochem. Mol. Biol. 30 (1995) 95–120.
[34] J. Hu, R.S. Sheng, Z.S. Xu, Ye. Zeng, Surface enhanced Raman spectroscopy of lysozyme, Spectrochim. Acta A. 51 (1995) 1087–1096.
[35] N.J. Greenfield, Using circular dichroism spectra to estimate protein secondary structure, Nat. Protoc. 1 (2006) 2876–2890.